In Situ Redox Microfluidic Synthesis of Core–Shell Nanoparticles and Their Long-Term Stability

9 **AUTHORS**, INCLUDING:

Yujun Song
University of Science and Technology Beijing
48 PUBLICATIONS   **883** CITATIONS

Xiaomiao Shen
Beihang University(BUAA)
5 PUBLICATIONS   **19** CITATIONS

Rongming Wang
University of Science and Technology Beijing
169 PUBLICATIONS   **4,463** CITATIONS

In Situ Redox Microfluidic Synthesis of Core–Shell Nanoparticles and Their Long-Term Stability

Yujun Song,*[,†] Shaoxia Ji,[†,∥] Yuan-Jun Song,[‡,∥] Runsheng Li,[†,∥] Jie Ding,[†,∥] Xiaomiao Shen,[†,∥] Rongming Wang,*[,‡] Riwei Xu,[§] and Xiaoyu Gu[§]

[†]Key Laboratory of Aerospace Advanced Materials & Performance (Ministry of Education) and School of Materials Science and Engineering, Beihang University, Beijing 100191, China

[‡]Key Laboratory of Micro-nano Measurement-Manipulation and Physics (Ministry of Education) and Department of Physics, Beihang University, Beijing 100191, China

[§]College of Materials Science and Engineering, Beijing University of Chemical Technology, Beijing 100029, China

ABSTRACT: An *in situ* redox process in microfluidic reactors was developed to synthesize hybrid nanoparticles with amorphous metallic cores and uniform metal oxide shells embedded with nanocrystallites at large scale. For example, the fabricated Fe(B)@iron oxides nanoparticles (NPs) exhibit permanent ferromagnetic properties at room temperature due to the strong magnetic coupling between different parts and the nanocrystalline pinning effect, providing an alternative design of nanostructures to break out the superparamagnetic limit in ultratiny particles. The NPs with amorphous metallic cores and uniform metal oxide shells can be well maintained over 4–5 months. The dictated novel microfluidic process provides a large-scale synthetic strategy for metal@metal oxide core–shell NPs with uniform shells and long-term stability and can be extended to a variety of material systems.

Samples	Elements	Content (Atom %)		
		Position 1[a]	Position 2[b]	Position 3[c]
Fresh	O	41.3 ± 3.9	78.6 ± 2.8	90.8 ± 1.6
	Fe	58.7 ± 3.9	21.4 ± 2.8	9.2 ± 1.6
Aged 30-45 days	O	41.8 ± 3.8	78.6 ± 2.8	90.8 ± 1.6
	Fe	58.6 ± 3.8	21.4 ± 2.8	9.2 ± 1.6
Aged 4-5 months	O	38.8 ± 2.4	77.1 ± 2.9	95.1 ± 1.2
	Fe	61.2 ± 2.4	22.9 ± 2.9	4.9 ± 1.2

1. INTRODUCTION

Hybridization of nanoarchitectures opens a new arena for nanoparticles (NPs) with multifunctions and novel physicochemical properties.[1–10] This innovative approach offers an efficient route overcoming undesirable conflicts with decrease in size, such as activity and stability,[1–3,6,8,11–13] superparamagnetism and ferromagnetism,[4,5,10] or sensitivity and intensity.[14–16] The application of new types of multifunctional NPs based on hybridization requires to overcome the mismatch among different components[7,17] and understand the inner-coupling and proximity effects in the constituent parts,[1,3–7,18] etc. In addition, it is essential to develop a controlled process for large-scale fabrication of hybrid nanostructures with long-term stability at different surroundings to fulfill their industrial perspective.[6,19–23]

For magnetic NPs, current efforts further concentrate on improving permanent hard magnets by beating superparamagnetism and performance degradation, which inhibits long-term ultrahigh-density data storage and future magnetic enhanced energy-harvesting technologies.[4,6,24] Progress in the construction of hybrid nanomaterials with core–shell structures promises to resolve these issues.[4,25] The exchange coupling and/or the unique exchange bias effect between two or more different magnetic phases in the cores and shells can provide an extra source of anisotropy energy overcoming thermal fluctuations, leading to magnetization stability.[4,25] The shell layers provide the protection of the core from oxidation and

corrosion in a more or less reactive atmosphere suitable for chemical stabilization.[4,6,7,26–29]

The large variety of magnetic exchanging couplings displayed by hybrid nanostructures is governed by interfaces and proximity effects among magnetic phases, which is related not only to their compositions and their reduced sizes but also to their geometrical structure levels and miscellaneous morphologies.[5,25,26] For stable magnetization at room temperature, it is essential to understand the exchange coupling in confined geometries and explore the influence of different surface and interfacial anisotropies for enhanced magnetic anisotropy energy.[4,25,4,30]

The prerequisite for the above study is the fabrication of core–shell NPs with confined geometrical structures and phases, particularly the shell part. However, formation of a structure well-defined shell on a highly curved sphere core by the traditional epitaxial growth is still nontrivial up to now since the more or less lattice mismatch between cores and shells is always existing.[6,17,18,29,31]

In the past decade, microfluidic reactors have caused much attention in the structure-controlled synthesis of NPs due to its *in situ* spatial and temporal reaction kinetics control as well as their easy scaling out.[7,10,19,29,32,33] Particularly, this process is feasible to fabricate the amorphous-phased metal oxide
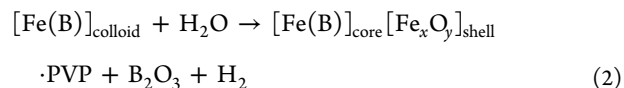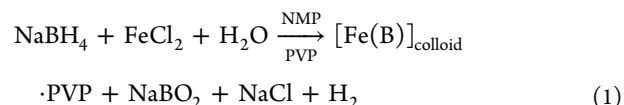
NPs,[20,27] which could preserve more active catalytic properties in the electrolysis of water than their crystalline species.[34] The amorphous phase may provide an alternative to avoid lattice mismatch issue if components in the hybrid nanostructures are all in amorphous phases due to their random arranged atoms. In addition, formation of amorphous−nanocrystalline composites for desired physicochemical properties can be easily controlled by regulating the annealing process of the amorphous precursors.[12,35,36] A similar phase transformation process has been used in the formation of single crystalline shells from amorphous precursors in Au@CdS NPs with large lattice mismatches.[17] Recently, the microfluidic process has been further extended to synthesize core−shell NPs with controlled structures and properties.[6,19,20,28,33,37−39,41] The results indicate that the shell thick and the related interfacial structures are crucial in the tuning of the physicochemical properties of these hybrid NPs.[6,20,27,28,33,40,41]

In this article, a generalized synthetic strategy using a microfluidic process has been further developed for large scale synthesis of core−shell nanoparticles (at least 2.6−5.2 g solid NPs/h). Amorphous core−shell NPs with metallic cores and uniform metal oxide shells are formed based on the novel organic−aqueous mixed phase reaction system. Such core−shell structures can last over 4−5 months even under ambient atmosphere. The relationship between the structure and property at various aging time was also investigated to disclosure the exchanging coupling among different magnetic phases for long-term magnetization stability.

2. EXPERIMENTAL SECTION

The $[Fe(B)]@Fe_xO_y$ core−shell NPs were synthesized by modifying our previous polyvinylpyrrolidone (PVP)-stabilized nanoparticle synthesis route.[28,41] There are two main modifications in the reaction. One is to dissolve the PVP and the metal salts into nanopure water to form the metal salts solution. Another is to dissolve the reducing agent $NaBH_4$ into the N-methyl-2-pyrrolidone to form the reducing agent solution. The $[Fe(B)]@Fe_xO_y$ NPs were formed according to the following reaction route. First, metal alloy NPs are formed by iron salt reduction stabilized by PVP as shown in reaction 1 using a microfluidic process (Scheme 1). Then the surface

metal atoms in the formed metal alloy cores are *in situ* oxidized into metal oxide (reaction 2) in the microfluidic reactor to form the shell of the NPs.

$$NaBH_4 + FeCl_2 + H_2O \xrightarrow[PVP]{NMP} [Fe(B)]_{colloid}$$

$$\cdot PVP + NaBO_2 + NaCl + H_2 \qquad (1)$$

$$[Fe(B)]_{colloid} + H_2O \rightarrow [Fe(B)]_{core}[Fe_xO_y]_{shell}$$

$$\cdot PVP + B_2O_3 + H_2 \qquad (2)$$

The experiment setup for the microfluidic process includes (Scheme 1): one syringe pump for the metal salt solution (a); one syringe pump for the reducing agent solution (b); two preheating stainless steel spirals immersed in the heating oil bath (inner diameter (i.d.) = 127 μm, length (L) = 15 cm) for the heating of the metal salt solution (c) and the reducing agent solution (d); one Y-mixer (i.d. = 500 μm) for the reactants to react to form nanoclusters; one microtubing (i.d. = 127 μm, L = 25−50 cm) for the nanocluster growth to NPs; and one product receiver protected by inert gas (i.e., N_2).

Briefly, PVP of 0.4 g (M_w = 10 000) and $FeCl_2 \cdot 4H_2O$ of 0.298 g (1.5 mmol) are dissolved into 50 mL of ultrapure water to form the metal salt solution. $NaBH_4$ of 0.156 g (4.0 mmol) is dissolved into 50 mL of NMP to form the reducing solution. Then the microfluidic synthesis is performed at 60−90 °C under inert atmosphere (nitrogen) protection using the following procedure: 20 mL of metal salt solution and 20 mL of reducing solution are sucked into each of the syringes and fixed in the platform of syringe pump, which is introduced into the Y mixer (e) to finish the nucleation by the syringe pump at a flow rate of 1.0 mL/min per pump, and then the solution enters into the microchannel (f) to finish the growth of NPs. The obtained fresh NP solution is collected in the product collector (g). The NPs are precipitated using centrifuge at a speed of 15 000 rpm for 20 min, and the top supernatant is decanted. The precipitated NPs are dissolved into the same volume of NMP. The centrifuge process is repeated twice, and the final black slurry in the bottle is dried under vacuum and kept in the desiccators for future use. Part of the sample is stored in the air or redissolved into DI water for the long-term stability evaluation. The core size and shell thickness of the NPs can be controlled by the reaction kinetic parameters. Higher iron salt to PVP ratio, higher $NaBH_4$ concentration, longer growth time (or the lower flow rate), and lower temperature (i.e., 60 °C) usually result into larger core size. The shell thickness can be controlled by the reaction temperature, the growth time, the collecting temperature, and $NaBH_4$ concentration. Longer growth time, lower reaction temperature, higher collecting temperature, and lower $NaBH_4$ concentration will result in thicker shells.

The particle size, shape, core−shell morphology, and crystal phase are examined transmission electronic microscopy (TEM). TEM investigations were performed on a Tecnai F20 (200 kV) electron microscope equipped with Gatan GIF 2000 energy filter system and energy dispersive X-ray spectrometry (EDX) produced by EDAX or conducted on a field emission transmission electron microscopy (JEM-3010, 300 kV, dot resolution: 0.17 nm). TEM samples were dispersed onto the grids by NP water or alcohol solution. The high-resolution (HR) TEM image of the sample reveals a clearly core−shell structure which is confirmed by the STEM-HAADF image (Z-contrast image). Crystal structures of NPs are

Scheme 1. Experimental Setup of the Integrated Tubular Microfluidic Reactor[a]
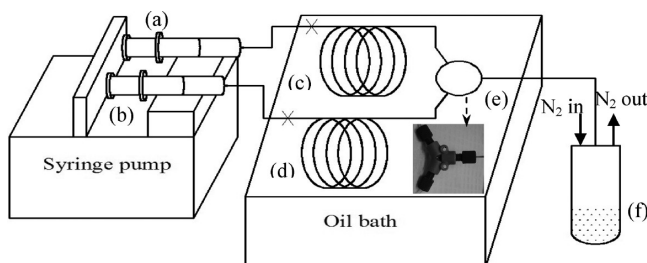
[a]a: One syringe pump for the metal salt solution; b: one syringe pump for the reducing agent solution; c: the preheating stainless steel spiral (inner diameter (i.d.) = 127 μm, length (L) = 15 cm) for the metal salt solution; d: the preheating stainless steel spiral (i.d. = 127 μm, L = 15 cm) for the reducing agent solution; e: the Y-mixer (i.d = 500 μm) for the reaction of nanoparticle formation; f: the microtubing (i.d. = 127 μm, L = 25−50 cm) for the nanoparticle growth; g: the product receiver.
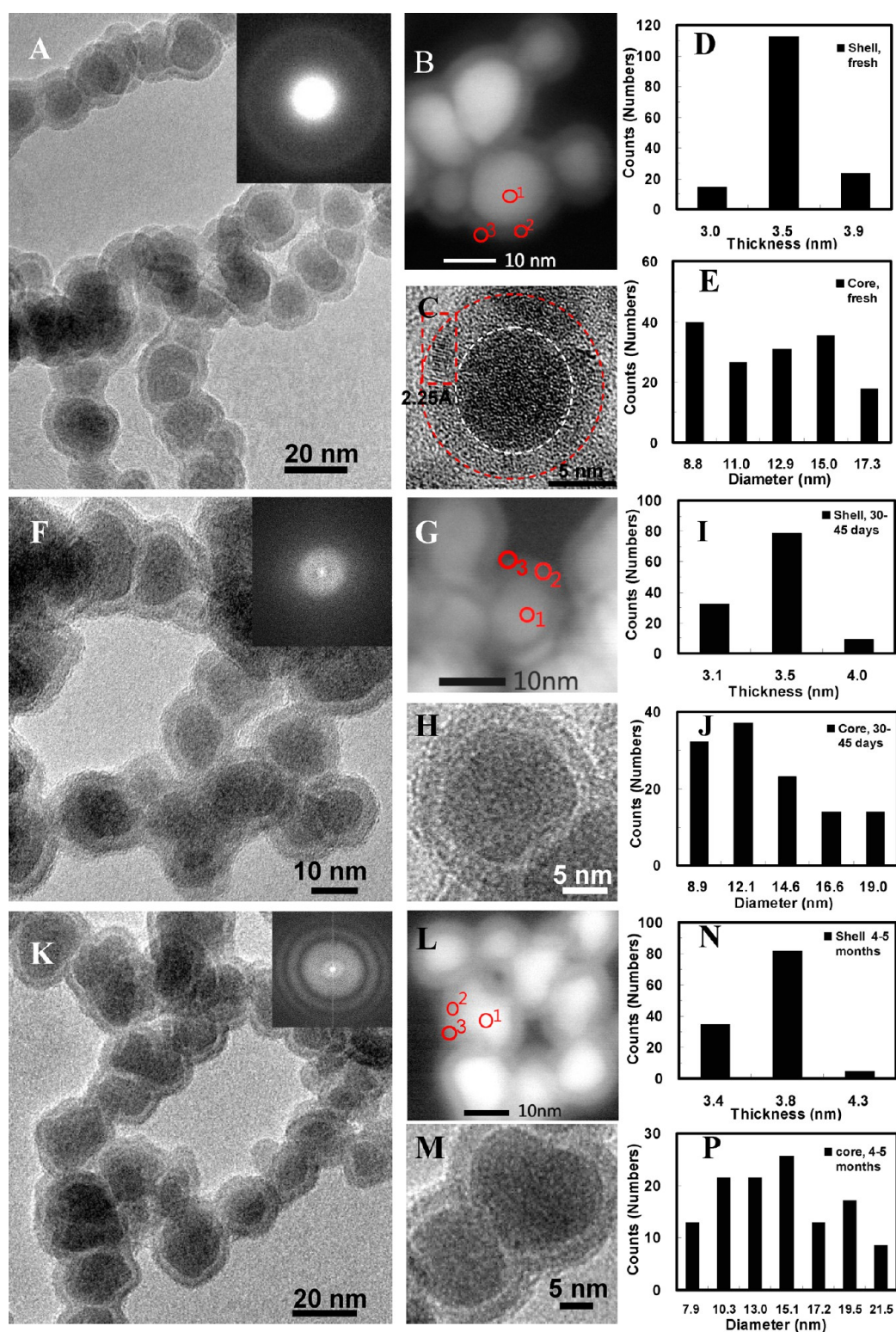
Figure 1. Core−shell morphology for the freshly prepared core−shell nanoparticles is demonstrated by the typical TEM image (A) and the Z-contrast STEM image (B), and one HR-TEM image for a single nanoparticle (C), whose shell thickness distribution and core size distribution are summarized in (D) and (E), respectively. Long-term stability in chemical composition and structure is evaluated by examining the core−shell morphology changes of those aged NPs by the typical TEM image (F: aged for 30−45 days; K: aged for 4−5 months), the Z-contrast STEM image (G: aged for 30−45 days; L: aged for 4−5 months), the HR-TEM image of one single core−shell nanoparticle (H: aged for 30−45 days; M: aged for 4−5 months), whose shell thickness distribution and core size distribution are summarized in (I) and (J) for NPs aged for 30−45 days, and N and P for NPs aged for 4−5 months. The inset in (A, F, K) is the SAED pattern of these core−shell nanoparticles. The marked red circles are positions for the element analysis by EDX.

evaluated by selected area electron diffraction (SAED) coupled in TEM and X-ray diffraction (XRD) using the copper Kα wavelength (λ = 1.540 56, Kα line, RINT2000) at a scanning rate of 3−4°/min.

The X-ray photoelectron spectroscopy (XPS) is used to determine the elemental composition as well as chemical and electronic state of the related elements in NPs by detecting their thin films. XPS measurements were carried out on an ESCALAB 250 Thermo Electron Corporation with an Al Kα X-ray source (1486.6 eV photons). The core-level signals were obtained at a photoelectron takeoff angle of 45° (with respect to the sample surface). The X-ray source was run at a power of 300 W. The samples were mounted on the standard sample studs by means of double-sided adhesive tapes. The pressure in the analysis chamber was maintained at 2×10^{-9} mbar during each measurement. To compensate for surface charging effects, all binding energies (BE's) are referenced to the C 1s hydrocarbon peak at 284.6 eV. The magnetic hysteresis loops of the samples at room temperature are obtained for the evaluation of their saturation magnetism (M_s), remanence (M_r), and coercivity (H_c) by a vibrating sample magnetometer (VSM, Lake Shore 7307). For the M versus T data, both zero field cooled (ZFC) and field cooled (FC) measurements for the fresh sample and the sample aged for 3 months are made with the temperature range from 2 to 350 K and the applied field of 100 Oe.

3. RESULTS AND DISCUSSION

Figure 1A is a typical TEM image for the fresh prepared NPs, clearly showing spherical core−shell morphology. The HAADF Z-contrast image (Figure 1B) illustrates ideal core−shell structural NPs with uniform shell ∼3.5 nm in thickness. It is interesting to observe one or two tiny crystallites of about 1−2 nm in most amorphous shells from their HR-TEM images as shown by one typical single NP (Figure 1C). The diameter distribution extracted from over 150 randomly selected individual NPs is depicted in Figure 1D,E. Statistics reveal that the shell thickness can be well-controlled to be 3.5 nm with deviation of only about 1−2 atomic layer thickness for various cores with diameter of 12.5 ± 3.1 nm, which is crucial in the control of the synergistic coupling for the core−shell NPs.

The long-term stability is one of the key features for the technological application of materials, especially for NPs. The long-term stability of their core−shell morphology up to 4−5 months has been conducted for the NPs. Figures 1F and 1K are typical TEM images for NPs exposed to the air for 30−45 days and 4−5 months, showing well-maintained core−shell structures. Their HAADF Z-contrast image (Figure 1G,L) illustrates ideal core−shell structural NPs with little changed uniform shell thickness as the fresh NPs (30−45 days: 3.41 nm; 4−5 months: 3.74 nm). The halo ring patterns of SAED (inset in Figure 1F,K) and HR-TEM images (Figure 1H,M) for single NPs indicate that their amorphous nature can be preserved perfectly even after exposing to air for several months. Surprisingly, those tiny crystallites in shells disappear after aging for more than several tens of days. The diameter distribution extracted from over 120 randomly selected individual NPs is depicted in Figure 1I,J for NPs aged for 30−45 days and in Figure 1N,P for NPs aged for 4−5 months. Statistics suggest that their shell thickness can be well-maintained in 3.41 nm (30−45 days) and 3.74 nm (4−5 months) with deviation of only ∼1−2 atomic layer thickness

for various cores, which is essential for the stable synergistic coupling in the core−shell NPs.

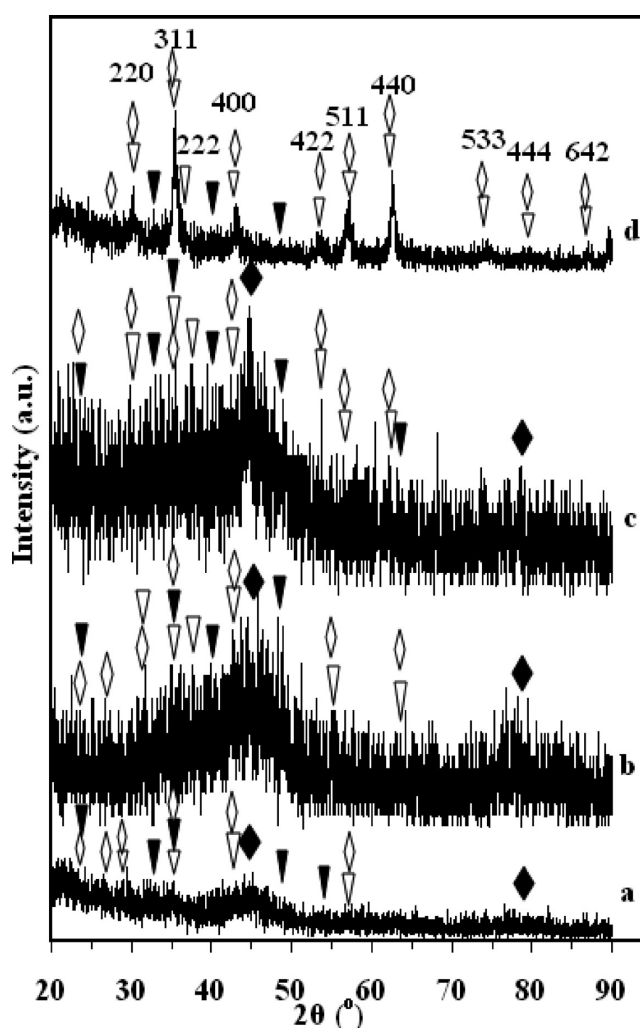Their structure stability is also evaluated by their XRD patterns (Figure 2). The XRD spectrum at low scanning rate

Figure 2. XRD patterns at a low scanning rate for the fresh prepared core−shell NPs (a), those aged for 30−45 days (b) and for 4−5 months (c), and those NPs (d) annealed at 100 °C overnight under nitrogen after reserving them in the aqueous solution for 15 days: (♦) Fe(B) alloys; (▽) Fe_3O_4; (◇) γ-Fe_2O_3; (▼) α-Fe_2O_3.

(2°/min) of the fresh-prepared NPs (Figure 2a) illustrates typical amorphous nature of the fresh Fe(B) NPs with one broad peak at 44.46° and one weak peak at 78.4° (solid diamonds).[12,35] Several detectable weak peaks can be possibly attributed to different types of iron oxides in shells due to the low S/N ratio. Weak peaks at 23.6°, 27.0°, 29.9°, 32.8°, 35.4°, 43.4°, 48.8°, 53.9°, and 57.2°, can be indexed as the (012) plane of α-Fe_2O_3 (PDF No. 33-0644) or the (210) plane of γ-Fe_2O_3 (PDF No. 39-1346), (213) plane of γ-Fe_2O_3, (220) plane of Fe_3O_4 or γ-Fe_2O_3, (104) plane of α-Fe_2O_3, (311) plane of Fe_3O_4 (PDF No. 79-0419), γ-Fe_2O_3 or (110) plane of α-Fe_2O_3, (400) plane of Fe_3O_4 or γ-Fe_2O_3, (024) plane of α-Fe_2O_3, (116) plane of α-Fe_2O_3, and (511) plane of Fe_3O_4 or γ-Fe_2O_3, respectively.[16,41−44] The selected area electron diffraction (SAED) (inset in Figure 1A) only shows the halo ring pattern, revealing mainly amorphous nature of these NPs. The aged NPs indicates that their amorphous Fe(B) features
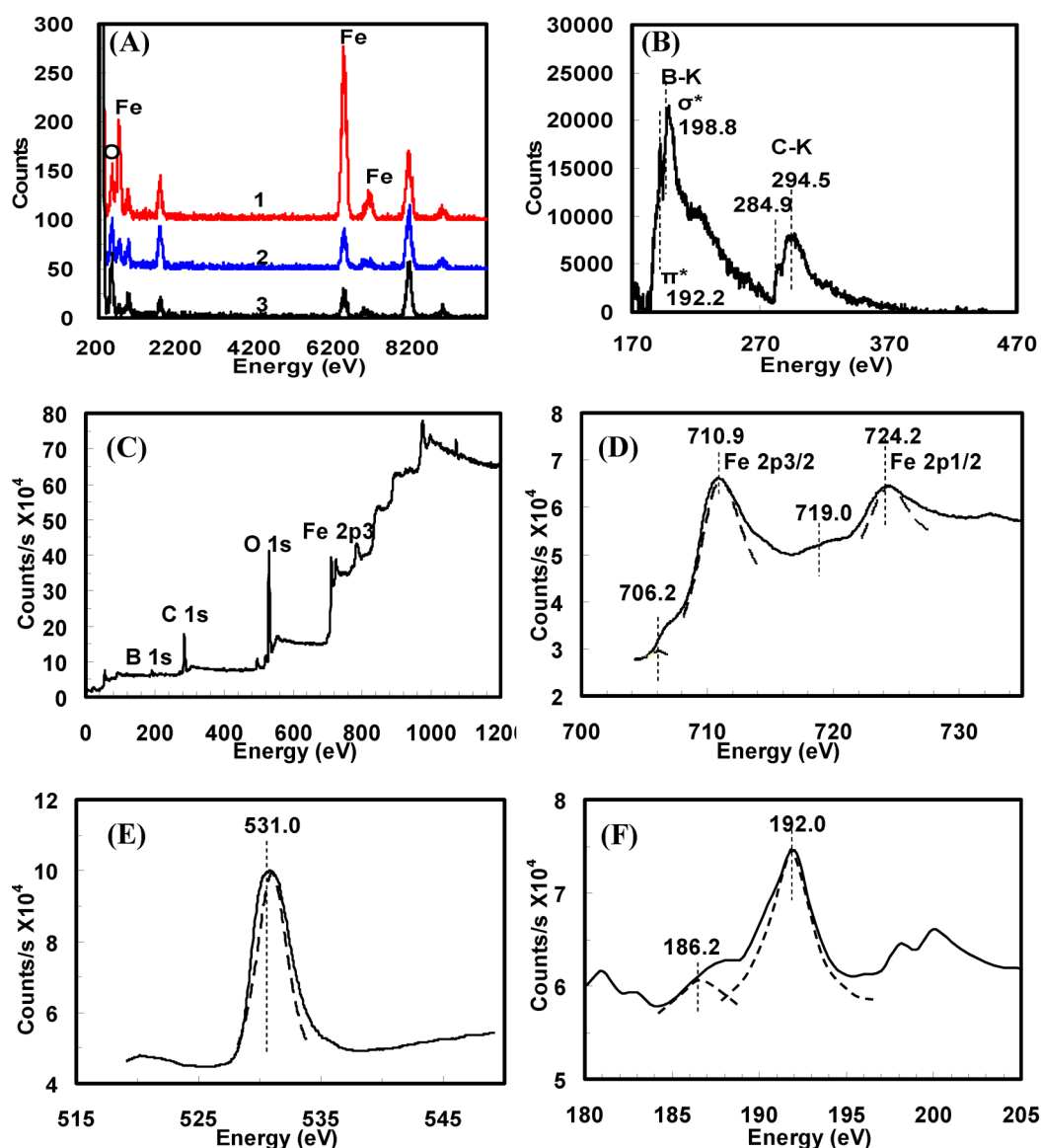
Figure 3. (A) Typical nanoscale area resolved EDX spectra recorded at the core center (1), the shell center (2), and the shell edge (3) of the fresh core−shell NPs. (B) EELS spectra of boron recorded for the fresh core−shell NPs. (C) Full XPS for the fresh NPs. (D) XPS of iron binding energy for the fresh NPs. (E) XPS of oxygen for the fresh NPs. (F) XPS of boron for the fresh NPs. The dashed lines in (D−F) are simulated peaks.

can be well-maintained over 4−5 months as evidenced by the broad halo peak at 45.3° and/or the broad weak peak at 78.7° (Figure 2b,c), which is consistent with the TEM results. There are still some possible weak peaks that can be attributed to different iron oxides, as indexed by the market symbols in their XRD patterns (solid triangles: α-Fe_2O_3; open triangles: γ-Fe_2O_3; open diamonds: Fe_3O_4). These core−shell structures can be maintained even in the aqueous solution for 15 days with gradually increased shell thickness. Further annealing at 100 °C under nitrogen promotes the crystallization of the thick shells of these NPs stored in the aqueous solution for 15 days. As shown in Figure 2d, their XRD pattern shows distinct peaks mainly for crystal Fe_3O_4 and/or γ-Fe_2O_3 (one featured weak peak: 27.0°, (213) plane; other peaks mixed with Fe_3O_4), and trace of α-Fe_2O_3 (featured peaks: 32.9°, (104) plane; 40.3°, (113) plane; 48.9°, (024) plane).[16,42−44]

Investigation indicates that these NPs mainly consist of Fe, O, and B by EDX (Figure 3A) and EELS (Figure 3B) analysis, whose changes in cores and shells can be used to examine the

composition stability of these NPs with elapsed time. Changes of Fe/O ratios (Table 1) through the core to the shell in the freshly prepared NPs was first investigated by EDX in STEM mode obtained from the core, the shell, and the edge of NPs (Figure 3A). The atomic ratio of O/Fe in the core (41.3/58.7, circle 1) is apparently lower than the stoichiometric ratio in Fe_3O_4 (4/3) or Fe_2O_3 (3/2) or FeO (1/1), indicating the metallic cores. The extremely higher oxygen content (O/Fe = 90.8/9.2) in the edge of the shell (circle 3) than the stoichiometric ratio of Fe_2O_3 reveals that the shells are obviously surrounded by lots of oxygen-content surfactants (e.g., PVP). The O/Fe atomic ratio in shells (78.6/21.4, circle 2) is still much higher than the stoichiometric ratio of Fe_2O_3 mainly due to the surfactant surrounding the NPs. Results on the O/Fe ratios in shells and the edge of shells also indicate that the iron can be completely oxidized in shells and the edge of shells, further confirming the existence of Fe_2O_3 as shown by their XRD spectrum. EELS analysis (Figure 3A) and EELS analysis of the whole NPs (Figure 3B) for typical fresh−

Table 1. Fe and O Contents at the Core Centers (Position 1), Shells (Position 2), and Shell Edges (Position 3) of the Fresh Core—Shell NPs and Those Aged for 30—45 days and 4—5 months Examined by EDX

samples	elements	content (atom %)		
		position 1[a]	position 2[b]	position 3[c]
fresh	O	41.3 ± 3.9	78.6 ± 2.8	90.8 ± 1.6
	Fe	58.7 ± 3.9	21.4 ± 2.8	9.2 ± 1.6
aged 30—45 days	O	41.8 ± 3.8	78.6 ± 2.8	90.8 ± 1.6
	Fe	58.6 ± 3.8	21.4 ± 2.8	9.2 ± 1.6
aged 4—5 months	O	38.8 ± 2.4	77.1 ± 2.9	95.1 ± 1.2
	Fe	61.2 ± 2.4	22.9 ± 2.9	4.9 ± 1.2

[a]The EDX recorded at position 1 refers to at the core centers of the single NPs as the circled point 1 of one single NPs in the Z-contrast images for those fresh prepared NPs, NPs aged for 30—45 days, and NPs aged for 4—5 months as shown in Figures 1C, 2C, and 2G, respectively. [b]The EDX recorded at position 2 refers to at the shell centers of the single NPs as the circled point 2 of one single NP in the Z-contrast images for those fresh prepared NPs, NPs aged for 1 month, and NPs aged for 5 months as shown in Figures 1C, 2C, and 2G, respectively. [c]The EDX recorded at position 3 refers to at the shell edges of the single NPs as the circled point 3 of one single NPs in the Z-contrast images for those fresh prepared NPs, NPs aged for 1 month, and NPs aged for 4—5 months as shown in Figures 1C, 2C, and 2G, respectively.

prepared NPs indicates that the NPs consist of boron besides Fe and O, revealing the existence of metallic Fe(B) cores as observed from their XRD spectrum, which is consistent with the proposal reaction mechanism (reactions 1 and 2).

The electronic structure of the consisting elements in the NPs can be well-characterized by XPS since the depth of the photoemitted electrons escaping from the very top surface of iron-based samples by the Al Kα X-ray source (1486.6 eV photons) is about 3.6 nm,[45,46] near their shell thickness (∼3.5 nm) of NPs. The full XPS spectrum for the fresh sample is plotted in Figure 3C, further confirming the existence of Fe, O, and B in these NPs. Figure 3D shows pronounced peaks at 710.9 and 724.2 eV, representing for Fe $2p_{3/2}$ and Fe $2p_{1/2}$.[45−48] Recalling the XRD pattern of the freshly prepared NPs, the weak satellite peak at ∼719.0 eV is possible from α-Fe_2O_3 in the shells.[45,48,49] The peak at 531.0 eV is mainly from oxygen in Fe_3O_4 (Figure 3E).[45,46] Combination of their XRD pattern (Figure 2a) and XPS analysis, the shells can be determined mainly as Fe_3O_4 and α-Fe_2O_3 and a possible trace of γ-Fe_2O_3. The shoulder at ∼706.2 eV (Figure 3D) can be dissolved, revealing the existence of metallic Fe, which can only be attributed to the metallic Fe(B) core.[45−48] The peaks at 192.0 and 186.2 eV for boron (Figure 3F) can be attributed to B_2O_3 and metallic boron (FeB) alloys, or Fe_3B.[47,48] Thus, the core can be determined as Fe(B) alloys. The B_2O_3 can be from the reoxidization of metallic boron diffused from the core to the surface of NPs.

Investigation indicates that Fe and O contents (Table 1) through the core to the shell examined by EDX in STEM mode (Figure 4A,B) can be well-maintained after aging for several tens of days. EELS analysis (Figure 4C) for those aged NPs suggests that boron can be well-stored in NPs even after they were washed by ultrapure water due to the shell formation.

The electronic structure of the consisting elements in the aged NPs can still be well-characterized by XPS since their shell thickness is ∼3.4—3.7 nm in the range of the detected depth of XPS. Compared with that of the fresh ones (Figure 6A-a), the
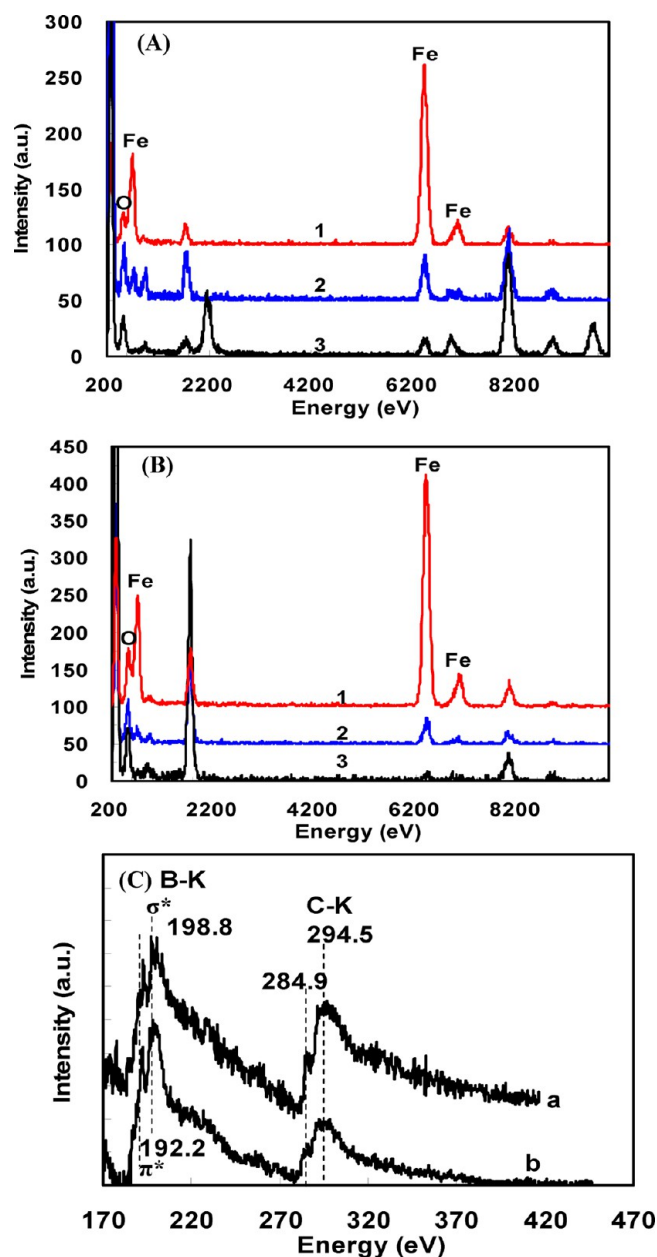

Figure 4. Typical nanoscale area resolved EDX spectra recorded at the core center (1), the shell center (2), and the shell edge (3) of the core—shell NPs aged for 1 month (A) and the core—shell NPs aged for 5 months (B). EELS spectra of boron recorded for the core—shell NPs (C) after aging for 30—45 days (a) and for 4—5 months (b).

boron peak of the NPs aged for 30—45 days shifts from 192.0 to 191.0 eV with a shoulder at 186.0 eV (Figure 5A-b), indicating more metallic boron in the aged NPs detectable by XPS. This result supports the deduction of the diffusion of boron from cores into shells, which can reduce some Fe^{2+} in shells to Fe^0, as shown by the relatively enhanced Fe^0 peak at 706.2 eV (Figure 5B-b). These results are consistent with the slightly reduced shell thickness in those NPs aged for 30—45 days. The excess boron can also benefit to the stability of the core—shell structure. These core—shell structures can be well-maintained for 4—5 months. At this stage, the B peak shifts to 189.9 eV with a shoulder at 192.0 eV (Figure 5A-c), suggesting the reoxidization of the boron in the metallic Fe(B), resulting in the increased shell thickness after aging for 4—5 months.
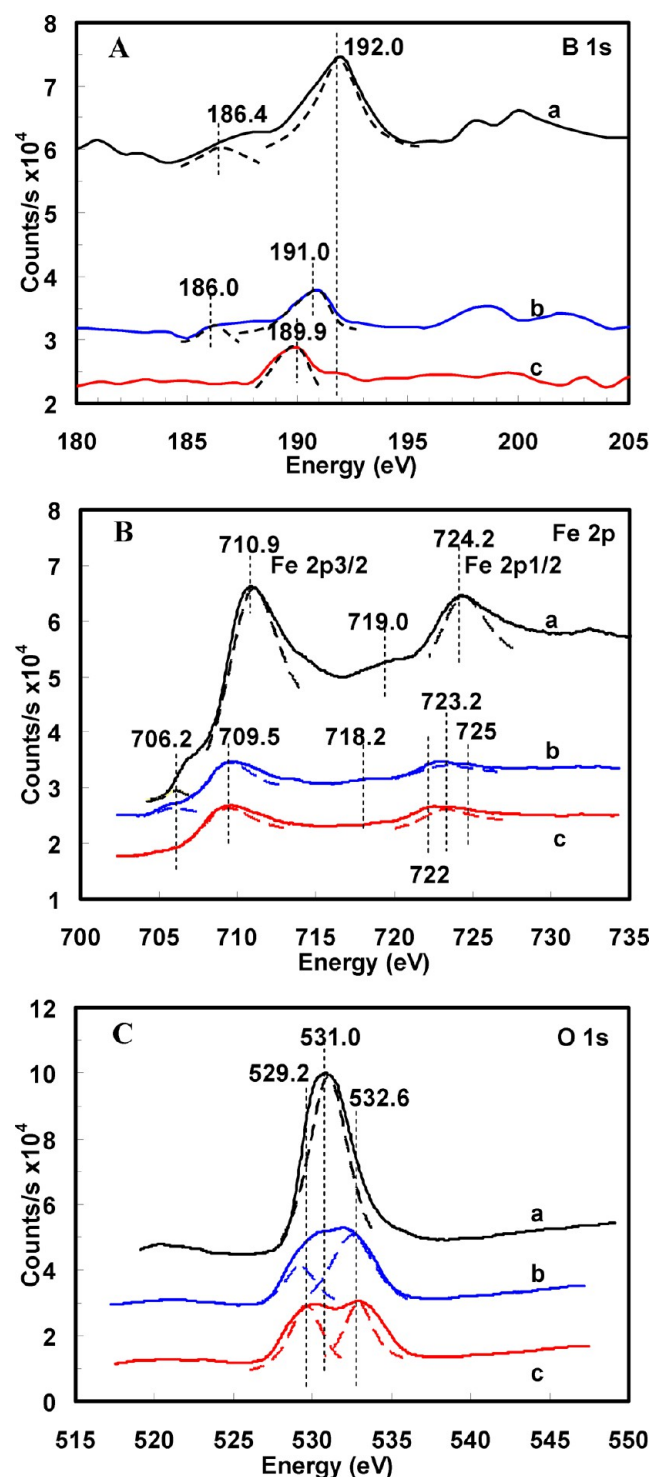
Figure 5. XPS spectra of the B 1s (A), the Fe 2p (B), and the O 1s (C) for the freshly prepared core−shell nanoparticles (a), for those aged for 30−45 days (b), for those aged for 4−5 months (c), and for those diluted NPs after aging for 4−5 months. The dashed lines are simulated peaks.
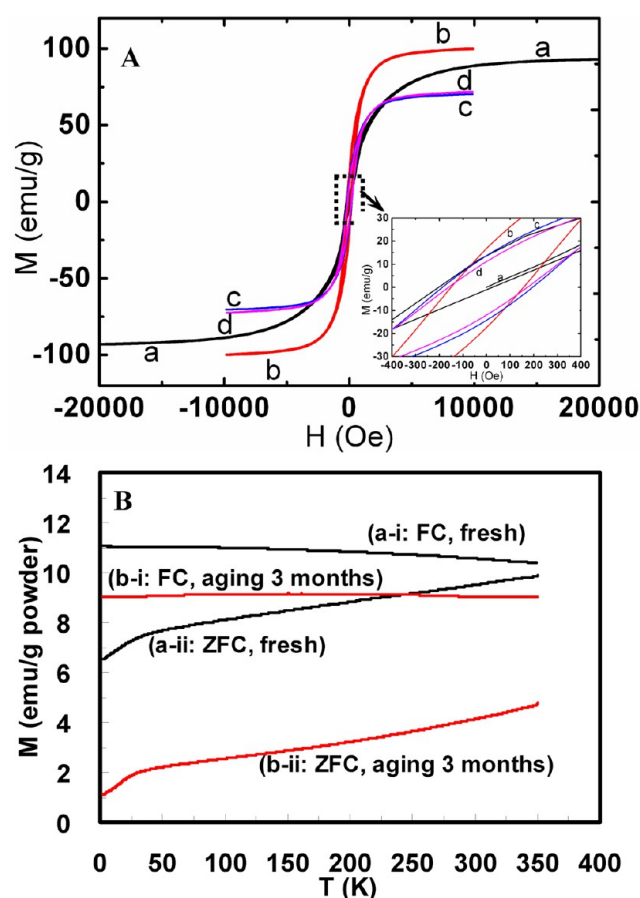

Figure 6. (A) Magnetic hysteresis loops at room temperature for the freshly prepared core−shell nanoparticles (a), the core shell nanoparticles aged for 30−45 days in air at room temperature (b), and the core−shell nanoparticles aged for 4−5 months in air at room temperature (c). Inset: magnified center range. All data are based on the effective solid content by heating the samples to 800 °C and kept for 30 min under N_2 flow to remove the impurity (e.g., the surfactant) using thermogravimetric analysis (TGA). (B) FC (a-i, b-i)−ZFC (a-ii, b-ii) curves for the fresh NPs (a) and the samples aged for 3 months (b). Note: the FC-ZFC data are based on all powder without normalization by the pure Fe(B)@iron oxide mass.

splitting of the peak at 724.2 eV (Figure 5B-b,c).[45,46] Interestingly, the Fe/B ratios (Table 2) by XPS in the age

Table 2. Fe/B Ratio Changes Based on the XPS Results on the Top 5−10 nm of the Thin Films Prepared by the Freshly Prepared NPs, the NPs after Aging for 30−45 days, and the NPs after Aging for 4−5 months

samples	fresh	aged 30−45 days	aged 4−5 months
Fe/B atom ratio	0.86	0.67	0.68

NPs film can be stable at about 0.67−0.68 up to 4−5 months. The reduced Fe/B ratio in the aged NPs than the fresh-prepared NPs can be attributed to the diffusion of B from cores to shells.

The dual peak feature of O 1s in NPs aged for 30−45 days (Figure 5C-b) and 4−5 months (Figure 5C-c) suggests existence of both oxygen from Fe_3O_4 (529.2 eV) and surface trapped oxygen (532.5 eV) that may prompt the formation of Fe^{3+} (from α-Fe_2O_3 and/or γ-Fe_2O_3),[48] consistent with those weak peaks from α-Fe_2O_3 and/or γ-Fe_2O_3 in their XRD

As the main element, the electronic structure of iron is crucial for the long-term stability of the NPs. XPS analysis reveals the formation of more Fe^{2+} during aging, which can be illustrated by the iron peak shift from 710.9 eV in the fresh NPs (Figure 5B-a) to 709.5 eV (the Fe^{2+} $2p_{3/2}$) in the aged ones (Figure 5B-b). Complex iron oxides can be detected from the

17280

dx.doi.org/10.1021/jp404402g | J. Phys. Chem. C 2013, 117, 17274−17284

Table 3. Magnetic Property of Fe(B)@Fe$_3$O$_4$ NPs before and after Aging

sample	M_s (emu/g)	M_r (emu/g)	M_r/M_s	H_c (Oe) left	H_c (Oe) right	H_e (Oe)	$H_{k,M}$ (Oe)	H_s (Oe)
as-synthesized	93	13.7	0.15	−208	−26	91	1350	19 958
aged for 30−45 days	100	16.7	0.17	−153	156	1.5	780	9879
aged for 4−5 months	70	14.3	0.20	−187	194	3.5	840	9871
diluted and aged for 4−5 months	72	12.0	0.17	−161	172	5.5	980	9872

patterns (Figure 2b,c). Considering the appearance of the iron satellite peak at 718.0 eV (Figure 5B-b) and the weak XRD peaks at 23.3° and 27.0° for the NPs aged for 30−45 days (Figure 2b), it can be deduced that surface-trapped oxygen can be consumed to form α-Fe$_2$O$_3$ at the early aging period, and then some of them transfer to γ-Fe$_2$O$_3$,[45,46,48] resulting in mixed iron oxides in the shell. This phenomenon can also be deduced from the XRD pattern of the NPs (Figure 2d) after aging in the aqueous solution where the enhanced oxidization process can occur.

The hybrid core−shell nanoarchitectures (particularly for the fresh NPs with amorphous shells embedded with tiny crystallites) endow them unique magnetic properties. Their room temperature hysteresis loops (Figure 6A:a−c) show monophase magnetic features. All of them exhibit typical permanent ferromagnetism with enough high remanence (M_r) and coercivity (H_c) (Table 3). These NPs can even maintain high saturation magnetism (70 emu/g) even after exposure in air for 4−5 months. Interestingly, the fresh NPs exhibit significant exchange bias (H_e: 91 Oe) at room temperature (Figure 6A-a) while those aged NPs show small exchange bias (Figure 6A:b,c), possibly due to the enhanced exchange coupling by the crystallites in shells. The enhanced exchange coupling in the fresh NPs can be further evidenced by their larger magnetic anisotropy ($H_{k,M}$: 1350 Oe) compared with those in the aged samples (780 and 840 Oe). The magnetic field anisotropy can be defined from the magnetization curves as the crossing point of linear extrapolations of the low field magnetization curve and the saturation curve[50] or the mean magnetic field of the crossing points based on the curves with the increased external magnetic field and the reduced magnetic field in this article if the magnetization curve does not pass the origin point. In addition, the external magnetic field to saturate the freshly prepared sample (H_s) is about 19 958 Oe, almost double those to saturate the aged samples (9871−9879 Oe, Table 3), suggesting that the aged samples become easier to reach saturation and more sensitive to the external field than the as-prepared NPs. At the initial aging period (30−45 days), the saturation magnetization of the freshly prepared sample is increased from 93 to 100 emu/g, possibly due to the formation of more metallic Fe^0 in NPs by the reducing effect of the diffusion boron into the shell (see the reduced shell thickness observed by TEM). With the continuous aging of these NPs, magnetic relaxation can occur together with the reoxidization of some Fe^0 into iron oxides (more iron oxides and thick shells), resulting in the M_s of the whole NPs decreasing from 100 to 70 emu/g (NPs aged for 4−5 months) and a slightly increased H_c.

Figure 6B is the zero-field cooling (ZFC) and field cooling (FC) curves for the fresh hybrid core−shell nanoarchitectures (Figure 6B-a) and those aged for 3 months (Figure 6B-b), indicating that the blocking temperatures (T_b) for the fresh or aged samples should be more than 350 K (77 °C). This result is consistent with those H_c results, clearly confirming these NPs

can maintain their permanent ferromagnetic property at temperatures as high as 77 °C.

Their TEM images for the freshly prepared NPs and those aged NPs also suggest that aggregation occurs, which is often observed for magnetic NPs during the preparation of the TEM grid by evaporation of the diluted NPs solution, particularly for those with large magnetism. In addition, the aggregation of these NPs seems to form chain-like structures, which is possibly the feature of these NPs synthesized in microfluidic channels due to the flow orientation effects.[41] This phenomenon also provides additional evidence that these NPs preserve the permanent ferromagnetic property at room temperature. Of course, the aggregation of these NPs indeed can affect their anisotropy and coercivity of the NP assembles as has been observed in the diluted Co@Au NPs and their concentrated species.[6] Theses NPs after aged for 4−5 months are diluted by 10 times in wax in order to reduce the interparticle interaction as much as possible, whose room temperature hysteresis loop is measured as shown in Figure 6A-d. These diluted NPs still exhibit typical permanent ferromagnetism (Table 3) with M_r of 10.8 emu/g, H_c from −161 to 174 Oe, and almost the same M_s (72 emu/g) as the nondiluted sample. The reduced H_c and slightly enhanced H_e and $H_{K,M}$ in these diluted NPs by comparing with those nondiluted NPs are clearly attributed to the reduced interparticle interaction.

Enlightened by the ferromagnetic−antiferromagnetic (FM−AFM) hybrid systems,[51−53] the magnetic behavior of our core−shell NPs can be elucidated by the competition between the related energy terms: the Zeeman energy (E_z), the anisotropy energy from the FM core (E_F), the anisotropy energy from the shell (E_{sh}), the anisotropy energy from the interparticle interactions |E_{inter}|, the ferrimagnetic (FI) shell (E_{FI}) and/or the tiny nanocrystallites in the shell ($E_{A,NA}$), the inner exchange energy at the FM−FI interface ($E_{inn,FM−FI}$), and the FI−NA ($E_{inn,FI−NA}$), the stress energy (E_{st}) in the NPs, etc. The E_{st} is from the flow shear on the formation of NPs in a microfluidic tubing, which usually increases the anisotropy energy. The magnetic domain structures in the amorphous shell, the amorphous core, and the small crystalline areas in the shell can be considered as separated single domains. The E_Z can be contributed from the ferromagnetic core ($E_{z,c}$), the ferrimagnetic shell ($E_{z,s}$), and tiny nanocrystallites (NA) in shells ($E_{z,NA}$). The effective Zeeman energy ($E_{Z,eff}$) is also related to the anisotropy energy from the FM core (E_F), or $E_{Z,eff} = (|E_Z| - |E_F|) = (|E_{z,c}| + |E_{z,s}| + |E_{z,NA}| - |E_F|)$. The effective anisotropy energy ($E_{A,eff}$) can be equal to ($|E_{FI}| + |E_{A,NA}| + |E_{st}| + |E_{sh}| + |E_{inter}|$), and the inner interfacial energy (E_{inner}) can be equal to ($|E_{inn,FM−FI}| + |E_{inn,FI−NA}|$). However, the $E_{Z,eff}$ for those NPs in this article (fresh and aged) is mainly dependent on $E_{z,c}$, $E_{z,s}$, $E_{z,NA}$, and |E_F| since the shape and interparticle interactions can be treated as almost the same according to their TEM images, and the goal in this article is only to study the magnetic stability of those particles aged or not.

17281

dx.doi.org/10.1021/jp404402g | J. Phys. Chem. C 2013, 117, 17274−17284

Obviously, $E_{A,eff}$ is more than E_{inner} for all samples, leading to enhanced coercivities, even though the $|E_{A,NA}|$ reduces to zero due to the disappearance of the nanocrystallites (NA) in shells and the $|E_{st}|$ can be reduced significantly after aging. Together with the large inner stress in the fresh samples, the nanocrystallites in shells as pinning sites can further slow down the rotation of spins.[6,50,51] The rotation of the FI spins in shells (including the spins in the tiny crystallites) cannot catch up with that of the FM spins in cores under an external field, leading to a distinct H_e. In the aged samples, E_A can be reduced due to the stress relaxation in NPs and the disappearance of the tiny crystallites (or no pinning effect) in shells according to their TEM images, as further evidenced by the much reduced $H_{k,M}$. Changes in E_{inner} may be balanced by the increased interface areas due to the increased core diameter and the disappearance of the tiny crystallites in shells. As a result, the exchange bias almost disappears in the aged NPs (only 2−3 Oe in NPs aged for 30−45 days and 3 Oe in NPs aged for 4−5 months). In addition, both the increased Fe(B) core volume (fresh: V_{core}/V_{shell} = 0.35; aged: V_{core}/V_{shell} = 0.39) and the inner stress relaxation are favorable for enhancing their M_s slightly.[17] As another result, the ZFC magnetization for the aged samples reduces more rapidly with the elapsed time (Figure 6B) than the FC magnetization, which can be attributed to the combined effect from the loss of the pining effect from the tiny crystallites in the shells, the magnetic relaxation in the aged samples (low M_s and high coercivity), and the relatively more ferrimagnetic iron oxide formed in shells (or less ferromagnetic Fe(B) in cores).

The developed *in situ* redox microfluidic process based on the reaction system of the aqueous metal salts solution and the organic reducing agent solution allows us to fabricate hybrid core−shell NPs with amorphous metallic cores and uniform metal oxide shells. The lattice mismatching in core−shell nanostructures formed by the conventional epitaxial growth process can be efficiently avoided due to the amorphous core and the amorphous shell.[19,38] Investigation of their core−shell structures and compositions changes with the exposure time in air indicates that the protection from the formed metal oxide shells, the interaction between cores and shells, and the existence of the metallic boron in cores contribute to their long-term stability. In addition, this process provides a method to induce large amount of metalloid element (i.e., B) into the NPs, which is essential to fabricate high-performance alloys by powder metallographic process. Because of the scaling-out and continuous reaction feature of the microfluidic process, this process itself preserves large-scale fabrication ability (∼2.6−5.2 g solid NPs/h for 10 parallel microchannels). We also examined the flexibility of this process by synthesis of other kinds of metallic cores and metal oxide shells by adding some other metal salts (e.g., $CoCl_2$, $SnCl_4$, $MnCl_2$, $AlCl_3$, $ZnCl_2$, etc.) with easily oxidized metals. It is found that other kinds of uniform metal oxide shells can be formed by this procedure, and the corresponding core−shell structures can last over 4 months.

Relationship between their structures and magnetic properties of the fabricated Fe(B)@Fe₃O₄ core−shell structures indicates that their typical permanent ferromagnetic properties can be attributed to the exchanging coupling interaction between cores and shells. Particularly, the significant exchange bias in the fresh NPs at room temperature can be reasonably attributed to the pinning effect from nanocrystallites in the shells and increased stress by the fluidic shear in microfluidic channels during the formation of NPs. All of them favor to increase the anisotropy energy in the NPs, which provide us a novel design of nanostructures (ferromagnetic cores and multiphased magnetic shells) to overcome the thermal fluctuations for long-term stable magnetization.

4. CONCLUSION

In conclusion, we have successfully developed an *in situ* redox process in microfluidic reactors for the continuous synthesis of amorphous nanostructures with metallic cores and metal oxide shells at large scale. The fabricated Fe(B)@Fe₃O₄ core−shell structures are found to last over 4−5 months. Investigation on their long-term stabilities suggests that the described synthesis process provides a large-scale synthetic strategy for various metallic core and metal oxide shell nanoparticles. Relationship between their structures and magnetic properties indicates that their typical permanent ferromagnetic properties can be attributed to the exchanging coupling interaction among cores shells and/or tiny crystallites in shells. The newly discovered hybrid nanostructural architecture formed by amorphous metallic cores and uniform shells decorated by pinning tiny crystallites described in this article provide an alternative to design nanostructures that can beat the "superparamagnetic limit" in ultratiny particles. In addition, the generalized synthetic strategy process could be used in the formation of other types of amorphous core−shell NPs that preserve tremendous applications such as catalysts superior to their crystalline species.

■ AUTHOR INFORMATION

Corresponding Author
*E-mail: songyj@buaa.edu.cn (Y.S.); rmwang@buaa.edu.cn (R.W.).

Author Contributions
‖S.J., Y.-J.S., R.L., J.D., and X.S. contributed to this article equally.

Notes
The authors declare no competing financial interest.

■ REFERENCES

(1) Zhang, J.; Tang, Y.; Lee, K.; Ouyang, M. Tailoring Light-Matter-Spin Interactions in Colloidal Hetero-nanostructures. *Nature* **2010**, *466*, 91−95.

(2) (a) Cozzoli, P. D.; Pellegrino, T.; Manna, L. Synthesis, Properties and Perspectives of Hybrid Nanocrystal Structures. *Chem. Soc. Rev.* **2006**, *35*, 1195−1208. (b) Duan, S.; Wang, R. Bimetallic Nanostructures with Magnetic and Noble Metals and Their Physicochemical Applications. *Progress in Natural Science: Materials International* **2013**, *23* (2), 113−126.

(3) Ruda, H. E.; Shik, A. Plasmon Phenomena and Luminescence Amplification in Nanocomposite Structures. *Phys. Rev. B* **2005**, *71*, 245328.

(4) Skumryev, V.; Stoyanov, S.; Zhang, Y.; Hadjipanayis; Givord, G. D.; Nogues, J. Beating the Superparamagnetic Limit with Exchange Bias. *Nature* **2003**, *423*, 850−855.

(5) Montero, M. I.; Liu, K.; Stoll, O. M.; Hoffmann, A.; Åkerman, J. J.; Martín, J. I.; Vicent, J. L.; Baker, S. M.; Russell, T. P.; Leighton, C.; Nogúes, J.; Schuller, I. K. Nanostructures and the Proximity Effect. *J. Phys. D: Appl. Phys.* **2002**, *35*, 2398−2402.

(6) Song, Y.; Ding, J.; Wang, Y. Shell Dependent Evolution of Optical and Magnetic Properties of Co@Au Core-Shell Nanoparticles. *J. Phys. Chem. C* **2012**, *116*, 11343−11350.

(7) Song, Y.; Wang, Y. H.; JI, S.; Ding, J. Shell-Driven Fine Structure Transition in Co@Au Core-Shell Nanoparticles. *Nano-Micro Lett.* **2012**, *4* (4), 235−242.

(8) Wen, T.; Krishnan, K. M. Thermal Stability and Morphological Transformations of Au_{core}-Co_{shell} Nanocrucibles. *J. Phys. Chem. C* **2010**, *114*, 14838−14842.

(9) Mohammad, F.; Balaji, G.; Weber, A.; Uppu, R. M.; Kumar, C. S. S. R. Influence of Gold Nanoshell on Hyperthermia of Superparamagnetic Iron Oxide Nanoparticles. *J. Phys. Chem. C* **2010**, *114*, 19194−19201.

(10) Ong, Q. K.; Lin, X.-M.; Wei, A. Role of Frozen Spins in the Exchange Anisotropy of Core-Shell $Fe@Fe_3O_4$ Nanoparticles. *J. Phys. Chem. C* **2011**, *115*, 2665−2672.

(11) Wang, R. M.; Dmitrieva, O.; Farle, M.; Dumpich, G.; Ye, H. Q.; Poppa, H.; Kilaas, R.; Kisielowsk, C. Layer Resolved Structural Relaxation at the Surface of Magnetic FePt Icosahedral Nanoparticles. *Phys. Rev. Lett.* **2008**, *100*, 017205.

(12) Tang, Z.; Song, Y.; Sun, S.; Zhang, T.; Jiang, Y. Magnetic Field Driving Gradient Effects on the Microstructure in Amorphous-nanocrystalline Cobalt Alloy Ribbons. *Nanoscale* **2012**, *4*, 386−393.

(13) Wang, R.; Zhang, H.; Farle, M.; Kisielowski, C. Structural Stability of Icosahedral FePt Nanoparticles. *Nanoscale* **2009**, *1*, 276−279.

(14) Carroll, K. J.; Hudgins, D. M.; Spurgeon, S.; Kemner, K. M.; Mishra, B.; Boyanov, M. I.; Brown, L. W., III; Taheri, M. L.; Carpenter, E. E. One-Pot Aqueous Synthesis of Fe and Ag Core/Shell Nanoparticles. *Chem. Mater.* **2010**, *22*, 6291−6296.

(15) Herman, D. A. J.; Ferguson, P.; Cheong, S.; Hermans, I. F.; Ruck, B. J.; Allan, K. M.; P, S.; Spencer, J. L.; Lendrum, C. D.; Tilley, R. D. Hot-Injection Synthesis of Iron/Iron Oxide Core/Shell Nanoparticles for T2 Contrast Enhancement in Magnetic Resonance Imaging. *Chem. Commun.* **2011**, *47*, 9221−9223.

(16) Song, Y.; Wang, R.; Rong, R.; Ding, J.; Liu, J.; Li, R.; Liu, Z.; Li, H.; Wang, X.; Zhang, J.; Fang, J. Synthesis of Well-dispersed Aqueous-Phase Magnetite Nanoparticles and Their Metabolism as MRI Contrast Agent for Reticuloendothelial System. *Eur. J. Inorg. Chem.* **2011**, 3303−3313.

(17) Zhang, J.; Tang, Y.; Lee, K.; Ouyang, M. Nonepitaxial Growth of Hybrid Core-Shell Nanostructures with Large Lattice Mismatches. *Science* **2010**, *327*, 1634−1638.

(18) Ong, Q. K.; Wei, A.; Lin, X.-M. Exchange Bias in Fe/Fe_3O_4 Core-Shell Nanoparticles Mediated by Frozen Interfacial Spins. *Phys. Rev. B* **2009**, *80*, 134418.

(19) Song, Y.; Kumar, C. S. S. R.; Hormes, J. Microfluidic Synthesis of Nanomaterials. *Small* **2008**, *4* (6), 698−711.

(20) Song, Y.; Henry, L. L.; Yang, W. T. Stable Cobalt Amorphous Nanoparticles Formed by an In-Situ Rapid Cooling Microfluidic Process. *Langmuir* **2009**, *25* (17), 10209−10217.

(21) Song, Y.; Wang, Y.; Li, B. B.; Fernandes, C.; Ruda, H. E. Interfacial Interaction Induced Self-Assembly of Nanoparticles into Superstructures. *Nanoscale* **2013**, *5* (15), 6779−6789.

(22) Nightingale, A. M.; deMello, J. C. Segmented Flow Reactors for Nanocrystal Synthesis. *Adv. Mater.* **2013**, *25*, 1813−1821.

(23) Song, Y.; Nallathamby, P. D.; Huang, T.; Elsayed-Ali, H. E.; Xu, X.-H. N. Correlation and Characterization of 3D Morphological Dependent Localized Surface Plasmon Resonance Spectra of Single Silver Nanoparticles Using Dark-Field Optical Microscopy and AFM. *J. Phys. Chem. C* **2010**, *114*, 74−81.

(24) Jones, N. The Pull on Stronger Magnets. *Nature* **2011**, *472*, 22−23.

(25) Eisenmenger, J.; Schuller, I. K. Overcoming Thermal Fluctuations. *Nat. Mater.* **2003**, *2*, 437−438.

(26) Fernández-García, M. P.; Gorria, P.; Blanco, J. A.; Fuertes, A. B.; Sevilla, M.; Boada, R.; Chaboy, J.; Schmool, D.; Grenèche, J.-M. Microstructure and Magnetism of Nanoparticles with γ-Fe Core Surrounded by α-Fe and Iron Oxide Shells. *Phys. Rev. B* **2010**, *81*, 094418.

(27) Song, Y.; Zhang, T.; Yang, W. T.; Albin, S.; Henry, L. L. Fine Crystal Structure Transition of Cobalt Nanoparticles Formed in a Microfluidic Reactor. *Cryst. Growth Des.* **2008**, *8* (10), 3766−3772.

(28) Song, Y.; Henry, L. L. Nearly Monodispersion CoSm Nanoparticles Synthesized by a Microfluidic reactor. *Nanoscale Res. Lett.* **2009**, *4*, 1130−1134.

(29) Cho, S.-J.; Idrobo, J.-C.; Olamit, J.; Liu, K.; Browning, N. D.; Kauzlarich, S. M. Growth Mechanisms and Oxidation Resistance of Gold-Coated Iron Nanoparticles. *Chem. Mater.* **2005**, *17*, 3181−3186.

(30) Zhou, Y. Z.; Chen, J. S.; Tay, B. K.; Hu, J. F.; Chow, G. M.; Liu, T.; Yang, P. Ni−NiO Core-Shell Nanoclusters with Cubic Shape by Nanocluster Beam Deposition. *Appl. Phys. Lett.* **2007**, *90*, 043111.

(31) Bao, Y.; Calderon, H.; Krishnan, K. M. Synthesis and Characterization of Magnetic-Optical Co-Au Core-Shell Nanoparticles. *J . Phys. Chem. C* **2007**, *111*, 1941−1944.

(32) Lee, W.-r.; Kim, M. G.; Choi, J.-r.; Park, J.-I.; Ko, S. J.; Oh, S. J.; Cheon, J. Redox-Transmetalation Process as a Generalized Synthetic Strategy for Core-Shell Magnetic Nanoparticles. *J. Am. Chem. Soc.* **2005**, *127*, 16090−16097.

(33) Park, J. I.; Saffari, A.; Kumar, S.; Gunther, A.; Kumacheva, E. Microfluidic Synthesis of Polymer and Inorganic Particulate Materials. *Annu. Rev. Mater. Res.* **2010**, *40*, 415−443.

(34) Smith, R. D. L.; Prévot, M. S.; Fagan, R. D.; Zhang, Z.; Sedach, P. A.; Siu, M. K. J.; Trudel, S.; Berlinguette, C. P. Photochemical Route for Accessing Amorphous Metal Oxide Materials for Water Oxidation Catalysis. *Science* **2013**, *340*, 60−63.

(35) Song, Y.; Li, Z.; Sun, Q.; Tang, Z.; Zhang, T.; Jiang, Y. Magnetic and Electric Property Evolution of Amorphous Cobalt-Rich Alloys Driven by Field Annealing. *J. Phys. D: Appl. Phys.* **2012**, *45*, 225001.

(36) Song, Y.; Sun, Q.; Jiang, Y.; Wang, S.; Fang, J.; Zhang, T. Crystallization of Cobalt Amorphous Alloys under Field Annealing. *J. Nanosci. Nanotechnol.* **2012**, *12*, 1074−1083.

(37) Sounart, T. L.; Safier, P. A.; Voigt, J. A.; Hoyt, J.; Tallant, D. R.; Matzke, C. M.; Michalske, T. A. Spatially-Resolved Analsysis of Nanoparticle Nucleation and Growth in a Microfluidic Reactor. *Lab Chip* **2007**, *7*, 908−911.

(38) deMello, A. J. Control and Detection of Chemical Reactions in Microfluidic Systems. *Nature* **2006**, *442* (27), 394−402.

(39) Zhao, B.; Moore, J. S.; Beebe, D. J. Sueface-Directed Liquid Flow Inside Microchannels. *Science* **2001**, *291*, 1023−1026.

(40) Song, Y.; Modrow, H.; Henry, L. L.; Saw, C. K.; Doomes, E. E.; Palshin, V.; Hormes, J.; Kumar, C. S. S. R. Microfluidic Synthesis of Cobalt Nanoparticles. *Chem. Mater.* **2006**, *18* (12), 2817−2827.

(41) (a) Song, Y.; Jin, P.; Zhang, T. Microfluidic Synthesis of Fe Nanoparticles. *Mater. Lett.* **2010**, *64*, 1789−1792. (b) Song, Y.; Sun, Q.; Zhang, T.; Jin, P. *J. Nanopart. Res.* **2010**, *12*, 2689−2697.

(42) Lv, B.; Xu, Y.; Wu, D.; Sun, Y. Preparation and Magnetic Properties of Spindle Porous Iron Nanoparticles. *Mater. Res. Bull.* **2009**, *44*, 961−965.

(43) Geng, B.; Tao, B.; Li, X.; Wei, W. Ni^{2+}/Surfactant-Assisted Route to porous α-Fe_2O_3 Nanoarchitectures. *Nanoscale* **2012**, *4*, 1671−1676.

(44) Hou, Y.; Xu, Z.; Sun, S. Controlled Synthesis and Chemical Conversions of FeO Nanoparticles. *Angew. Chem., Int. Ed.* **2007**, *46*, 6329−6332.

(45) Wagner, C. D.; Naumkin, A. V.; Kraut-Vass, A.; Allison, J. W.; Powell, C. J.; Rumble, J. R. J. *NIST Standard Reference Database 20, Version 3.5.* Distributed by the Measurement Services Division of the National Institute of Standards and Technology (NIST) Material Measurement Laboratory (MML), 2003.

(46) Grosvenor, A. P.; Kobe, B. A.; Biesinger, M. C.; S, M. N. Investigation of Multiplet Splitting of Fe 2P XPS Spectra and Bonding in Iron Compounds. *Surf. Interface Anal.* **2004**, *36*, 1564−1574.

(47) Sharma, S. K.; Hofmann, S. Study of Amorphous and Crystallized by Auger Electron Spectroscopy and X-ray Photoelectron Spectroscopy. *Appl. Surf. Sci.* **1991**, *51*, 139−155.

(48) Fujii, T.; de Groot, F. M. F.; Sawatzky, G. A.; Voogt, F. C.; Hibma, T.; Okada, K. In Situ XPS Analysis of Various Iron Oxide Films Grown by NO_2-Assisted Molecular-Beam Epitaxy. *Phys. Rev. B* **1999**, *59* (4), 3195−3201.

(49) Yamashita, T.; Hayes, P. Analysis of XPS Spectra of Fe^{2+} and Fe^{3+} Ions in Oxide Materials. *Appl. Surf. Sci.* **2008**, *254*, 2441−2449.

(50) Song, Y.; Sun, S.; Zhang, T.; Jin, P.; Han, L. Synthesis of Worm and Chain-like Nanoparticles by a Microfluidic Reactor Process. *J. Nanopart. Res.* **2010**, *12*, 2689−2697.

(51) Crangle, J.; Goodman, G. M. The Magnetization of Pure Iron and Nickel. *Proc. R. Soc. London, Ser. A* **1971**, *321* (1547), 477−491.

(52) Caruntu, D.; Caruntu, G.; O'Connor, C. J. Magnetic Properties of Variable-Sized Fe_3O_4 Nanoparticles Synthesized from Non-Aqueous Homogeneous Solutions of Polyols. *J. Phys. D: Appl. Phys.* **2007**, *40*, 5801−5809.

(53) Dobrynin, A. N.; Levlev, D. N.; Temst, K.; Lievens, P.; Margueritat, J.; Gonzalo, J.; Afonso, C. N.; Zhou, S. Q.; Vantomme, A.; Piscopiello, E.; Van Tendeloo, G. Critical Size for Exchange Bias in Ferromagnetic-Antiferromagnetic Particles. *Appl. Phys. Lett.* **2005**, *87*, 012501.

17284

dx.doi.org/10.1021/jp404402g | *J. Phys. Chem. C* 2013, 117, 17274−17284